

Defect-rich spinel ferrites with improved charge collection properties for efficient solar water splitting

Runfa Tan^{a,b}, Yoo Jae Jeong^{a,b}, Qu Li^{a,b}, Minje Kang^{a,b}, In Sun Cho^{a,b,*}

^aDepartment of Materials Science & Engineering, Ajou University, Suwon 16499, Republic of Korea

^bDepartment of Energy Systems Research, Ajou University, Suwon 16499, Republic of Korea

Received: September 19, 2022; Revised: November 11, 2022; Accepted: December 16, 2022

© The Author(s) 2022.

Abstract: Spinel zinc ferrite (ZnFe₂O₄, ZFO) is a potential photoanode material for photoelectrochemical (PEC) water splitting because of its ideal bandgap (1.9–2.1 eV) and superior chemical stability in aqueous solutions. However, the low charge collection efficiency significantly hinders the improvement in PEC activity. Herein, we report an ultrafast and effective flame activation route to enhance the charge collection properties of ZFO. First, high-temperature flame (> 1300 °C) facilitated surface and grain boundary diffusions, increasing the grain size and connectivity of the ZFO nanoparticles. Second, the reducing atmosphere of the flame enabled the formation of surface defects (oxygen vacancy and Fe²⁺), thereby increasing the charge carrier density and surface adsorption sites. Significantly, these two factors promoted charge transport and transfer kinetics, resulting in a 10-fold increase in the photocurrent density over the unactivated ZFO. Furthermore, we deposited a thin Al₂O₃ overlayer to passivate the ZFO surface and then the NiFeO_x oxygen evolution catalyst (OEC) to expedite hole injection into the electrolyte. This surface passivation and OEC deposition led to a remarkable photocurrent density of ~1 mA/cm² at 1.23 V versus the reversible hydrogen electrode, which is the highest value among all reported ZFO photoanodes. Notably, the NiFeO_x/Al₂O₃/F-ZFO photoanode achieved excellent photocurrent stability over 55 h (96% retention) and superior faradaic efficiency (FE > 94%). Our flame activation method is also effective in improving the photocurrent densities of other spinel ferrites: CuFe₂O₄ (93 times), MgFe₂O₄ (16 times), and NiFe₂O₄ (12 times).

Keywords: spinel ferrites; flame activation; defect-rich surface; charge collection; photoelectrochemical (PEC); water splitting

1 Introduction

Solar radiation is the most prominent energy source on the Earth. Hence, efficient utilization of sunlight is critical for a sustainable, carbon-neutral, and global energy economy [1,2]. Hydrogen production via photoelectrochemical

(PEC) water splitting is an effective method to counter current environmental and energy issues [3,4]. However, the solar-to-hydrogen (STH) efficiencies of the current PEC systems remain far below 10%, limiting the commercial viability. The key obstacle is the lack of efficient photoelectrodes [5,6].

Metal oxides have received significant attention as photoelectrodes owing to their excellent durability, non-toxicity, and abundance. Consequently, numerous metal oxide semiconductors, including TiO₂, WO₃, Fe₂O₃,

* Corresponding author.

E-mail: insuncho@ajou.ac.kr

and BiVO₄, have been extensively investigated [7–16]. During the last decade, unprecedented rapid progress has been made; however, their relatively wide bandgap and poor charge collection (separation, transport, and transfer) properties limit their practical applications [6]. Therefore, developing new oxides that can absorb a large fraction of the solar spectrum and efficiently drive water splitting is urgently required.

Spinel ferrites (MFe₂O₄, M = Zn, Ca, Mg, Cu) are ternary oxide compounds formed by trivalent iron and divalent metal ions that constitute tetrahedral and octahedral sites [17], which have recently gained increasing interest for PEC water splitting owing to their ideal bandgap (1.9–2.1 eV), excellent thermal and chemical stability, and abundance [18–26]. In particular, zinc ferrite (ZnFe₂O₄, ZFO) is the most investigated photoanode material [27,28] because of its suitable valence band edge position and high theoretical STH efficiency (~21%), which is substantially higher than the values predicted for Fe₂O₃ (~15%), BiVO₄ (~9%), WO₃ (~6%), and TiO₂ (~2%). However, ZFO has several intrinsic limitations [29–31]: (1) small light absorption coefficients, (2) short minority carrier diffusion length, (3) poor electron mobility owing to the hopping mechanism of localized d-electrons in FeO₆ octahedra, and (4) slow surface reaction kinetics. In addition, from a synthesis point of view, the high crystallization temperatures (above 1000 °C) limit their synthesis on a heat-sensitive transparent conductive oxide substrate [32].

Several strategies have been considered to improve the PEC performance of ZFO photoanodes. For instance, Zhu *et al.* [20] investigated the influence of cation disordering in ZFO nanorod arrays (NRs) on the charge separation and injection efficiency, demonstrating a new benchmark photocurrent density of approximately 1.0 mA/cm² at 1.23 V vs. the reversible hydrogen electrode (1.23 V_{RHE}) [20]. Anushkaran *et al.* [33] construct a SiO_x hole transport channel on ZFO, achieving a 0.57 mA/cm² photocurrent density at 1.23 V_{RHE}. Guo *et al.* [34] introduced Ti⁴⁺ doping into the ZFO nanoparticle film to increase the charge carrier concentration and promote charge transport, achieving a photocurrent density of 0.35 mA/cm² at 1.23 V_{RHE}. Kim *et al.* [35,36] utilized a multiple modification strategy (hybrid microwave annealing, insertion of a TiO₂ underlayer, and Ti⁴⁺ doping) to effectively suppress charge-carrier recombination in ZFO NRs, resulting in a 37-fold increase in the photocurrent density. Recently, Polo *et al.* [37] showed that film

thickness, annealing temperature, and n-type doping are the most crucial factors affecting the PEC performance of ZFO, providing further insight into developing an efficient ZFO photoanode. All these reports indicate that simultaneous optimization in the charge transport and transfer (i.e., charge collection) process should be considered to improve the PEC activity effectively.

In this study, we demonstrate a flame activation method using a ZFO nanoparticle film to effectively improve the charge collection property without any complex procedures or vacuum systems. Flame activation strategy has been reported as a route to produce oxygen vacancy in WO₃, BiVO₄ [38–40]. However, this work is the first time to apply the flame strategy on the promising ZFO photoanode and study the flame effect on the photoelectrochemical behavior. A high-temperature flame with a reducing atmosphere significantly influences the physicochemical properties, such as grain size, connectivity, and defect formation of ZFO nanoparticle films. In addition, rapid treatment within 1 min minimizes substrate damage. Significantly, the flame treatment effectively promoted charge transport and transfer kinetics, allowing a large increase in the water-splitting photocurrent density over untreated ZFO. Moreover, we demonstrated a high FE (> 94%) and excellent photocurrent stability (> 96% retention after 55 h) by combining an Al₂O₃ overlayer and NiFeO_x OEC. Finally, we showed that the flame activation method effectively improves the photocurrent densities of other spinel ferrites (CuFe₂O₄, MgFe₂O₄, and NiFe₂O₄).

2 Experimental

2.1 Synthesis of ZnFe₂O₄ (ZFO) nanoparticle film

The ZFO nanoparticle film was deposited using a sol-gel spin-coating method. First, a 0.4 M precursor coating solution was prepared by dissolving the 1.190 g Zn(NO₃)₂·6H₂O (98%; Alfa-Aesar, MA, USA) and 3.232 g Fe(NO₃)₃·9H₂O (98.5%; Kanto Chemical, Tokyo, Japan) in 10 mL 2-methoxyethanol (99.3%; Alfa-Aesar), followed by ultrasonication for 10 min. Subsequently, 0.2 mL acetylacetone (99%; Sigma-Aldrich, MO, USA) was added dropwise to the solution, and the ultrasonication treatment was continued for 10 min, followed by aging for 12 h with magnetic stirring at 25 °C. Notably, the addition of acetylacetone led to the high stability of the coating solution, thereby enabling uniform film coverage. Next, the resultant coating solution was spun onto a

pre-cleaned fluorine-doped tin oxide (FTO) substrate at 2500 r/min for 1 min and then pre-annealed at 250 °C for 10 min on a hot plate. Finally, the obtained film was annealed in a box furnace at 550 °C for 2 h at a 5 °C/min ramping rate to synthesize a crystalline ZFO nanoparticle film.

2.2 Flame activation method

The flame activation process was conducted using flame surface processing equipment (IFLA-500, Applied Plasma Inc., Gumi City, Republic of Korea). Liquefied petroleum gas (LPG; 50% butane and 50% propane) and compressed air from a Kolavo air compressor (Seoul, Republic of Korea) were used as the fuel and oxidizer, respectively. The fuel-to-oxygen equivalence ratio (Φ) of the premixed flame was controlled by varying the air flow rate. Notably, Φ controls the flame atmosphere: a flame with $\Phi > 1$ (fuel-rich condition) produces a reducing environment, while a flame with $\Phi < 1$ (fuel-lean condition) produces an oxidizing environment [41,42]. The optimized LPG and air flow rates were 5 and 130 mL/min, respectively, to generate a reducing environment ($\Phi = 1.05$). Flame activation of the ZFO photoanode was conducted inside the flame for 30 s.

2.3 Deposition of Al₂O₃ and NiFeO_x layers

For the Al₂O₃ and NiFeO_x OEC layer deposition, the aluminum nitrate nonahydrate ($\geq 98\%$; Sigma-Aldrich, MO, USA), nickel (II) nitrate hexahydrate ($\geq 98.5\%$; Sigma-Aldrich, MO, USA), iron (III) nitrate nonahydrate, and 2-methoxyethanol were used to prepare a 0.01 M Al₂O₃ and 0.02 M NiFeO_x coating solution. The ZFO photoanode was dipped into the Al₂O₃ coating solution for 5 s and withdrawn vertically at a constant speed, then annealed at 200 °C for 10 min on the hotplate; this process was repeated three times. The NiFeO_x OEC was deposited using a previously reported method [43]. Briefly, Ni(NO₃)₂·3H₂O and Fe(NO₃)₂·3H₂O were dissolved in 2-methoxyethanol to produce a 0.02 M precursor solution (Ni:Fe = 6:4). Next, the Al₂O₃/F-ZFO samples were soaked in the mixed solution for 5 min. Finally, the samples were dried in an oven (60 °C) for 10 min, and then rinsed with a 1 M KOH solution for 10 s.

2.4 Material characterizations

The crystalline structures and phases of the samples

were analyzed using the X-ray diffractometer (D/MAX-Ultima III, Rigaku, Tokyo, Japan) and the Raman spectroscope (alpha300 R, WITec, Ulm, Germany). A 532 nm excitation wavelength laser was used for Raman spectroscopy. The morphology and thickness of the samples were examined using the scanning electron microscope (SEM; JSM-IT500HR, Jeol, Tokyo, Japan). The samples' surface compositions and oxygen vacancies were investigated using X-ray photoelectron spectroscope (XPS; ESCALAB 250, Thermo Fisher Scientific, MA, USA) and electron paramagnetic resonance spectrometer (JES-FA100, JEOL). EPR measurements were conducted using a JES-FA100 (JEOL) system in the X band using a frequency of 9.4 GHz with a power of 2 mW. The optical properties of the samples were recorded using an ultraviolet–visible–near infrared spectrophotometer (UV-2600i, Shimadzu Scientific, Kyoto, Japan) with an integrating sphere. The photoluminescence (PL) and time-resolved transient PL (TRPL) spectra of the samples were measured using a Fluorolog-3 spectrophotofluorometer (HORIBA, Kyoto, Japan) with a 374 nm excitation wavelength. The electrical conductivity (Fig. S3 in the ESM) was measured by the Hall effect measurement system (Ecopia, HMS-3000). Atomic force microscopy (Asylum Research, MFP-3D SPM) was used to study the flame effect on bare FTO (Fig. S4 in the ESM).

2.5 (Photo)electrochemical measurements

PEC and electrochemical measurements of the samples were performed using a potentiostat (SP-200, BioLogic, Claix, France) in a three-electrode system with ZFO, a platinum wire, and Ag/AgCl (3 M KCl) as the working, counter, and reference electrodes, respectively. A solar simulator (LCS-100, Newport, CA, USA) was used as the illumination source. Before the measurement, the solar simulator intensity (AM1.5G, 100 mW/cm²) was calibrated using a reference cell (Mode 91150V, Newport, CA, USA). A 1 M NaOH solution (pH = 13.6) was used as the electrolyte.

The photocurrent density–potential (J – V) curve was obtained via linear sweep voltammetry measurements at a 50 mV/s scan rate under dark and light conditions. The reference electrode potential was converted to a RHE scale using Eq. (1):

$$V_{\text{RHE}} = V_{\text{Ag/AgCl}} + (0.059 \times \text{pH}) + E_{\text{Ag/AgCl}}^{\circ} \quad (1)$$

where $V_{\text{Ag/AgCl}}$ is the applied bias and $E_{\text{Ag/AgCl}}^{\circ}$ is the standard hydrogen electrode potential of the Ag/AgCl

electrode at 298 K [40].

Electrochemical impedance spectroscopy (EIS) spectra were recorded in the frequency range of 1 MHz–1 Hz at an applied bias potential of 1.23 V_{RHE} under simulated sunlight illumination. The electrochemical active surface area (EASA) of the samples was evaluated by measuring the cyclic voltammograms at scan rates of 100, 200, 300, 400, and 500 mV/s. Mott–Schottky measurements were performed in the dark at a frequency of 1 kHz and then plotted based on Eq. (2):

$$\frac{1}{C^2} = \frac{2}{\varepsilon_0 \varepsilon_r A^2 e N_D} \left(V - V_{fb} - \frac{kT}{e} \right) \quad (2)$$

where C is the space charge capacitance, N_D is the donor density, ε_0 is the permittivity of vacuum (8.854×10^{-19} F/m), ε_r is the dielectric constant, A is the surface area of the film (0.11 cm^2), V is the applied potential, V_{fb} is the flat band potential, k is the Boltzmann constant (1.381×10^{-23} J/K), e is the electron charge (1.602×10^{-19} C), and T is the absolute temperature. A dielectric constant of $\varepsilon_r = 80$ was used for ZFO [44].

3 Results and discussion

3.1 Synthesis and flame activation of ZFO

The ZFO nanoparticle film was synthesized using a sol–gel spin-coating method (Fig. S1 in the ESM). First, the ZFO coating solution was spun onto FTO substrates, followed by pre-annealing at 250 °C to allow evaporation of the solvent and decomposition of the gel film. Subsequently, the pre-annealed film was annealed at 550 °C to obtain a nanocrystalline ZFO film. Finally, the flame treatment was conducted to promote the PEC activity of ZFO. Figure 1(a) illustrates the flame activation process. The ZFO film was rapidly inserted into the stable flame zone (> 1300 °C) and maintained for 30 s (Fig. S2 in the ESM). Notably, the flame was produced under fuel-rich conditions (equivalence ratio $\Phi > 1$) that created reducing gases of CO and H₂, which directly contacted the ZFO surface and then reacted with lattice oxygen to effectively generate oxygen vacancies [42].

The SEM images of ZFO and flame-activated ZFO (F-ZFO) are shown in Figs. 1(b) and 1(c). Both ZFO and F-ZFO exhibited approximately 600 nm thick nanoparticle film with uniform coverage. In addition, energy dispersive spectroscopy elemental mapping

analysis indicates that Zn and Fe have an approximate 1:2 stoichiometric ratio and uniform distributions throughout the entire film (Fig. S5 in the ESM). The average grain size of ZFO was determined to be ~ 40 nm from the top-view SEM image. Notably, multiple voids and pores were observed in the ZFO layer, which was caused by the insufficient grain growth and fusion due to the low annealing temperature (550 °C). In contrast, F-ZFO exhibited two times larger (~ 82 nm) and well-connected grains. The top-view SEM images clearly revealed that the grain size and connectivity increased. Furthermore, the voids and pores disappeared, particularly in the vicinity of the F-ZFO and FTO interface (Fig. 1(c)). Generally, high-temperature annealing is beneficial for grain boundaries and surface diffusion, hence facilitating grain growth and fusion [45,46]. Therefore, the high-temperature flame process induced larger grains, high connectivity, and reduced porosity in F-ZFO, which could improve the charge transport properties (Fig. S6 in the ESM). Additionally, despite the high-temperature treatment (> 1300 °C), the FTO appeared undamaged, another benefit of the flame activation method.

The phase compositions and crystal structures of ZFO and F-ZFO were evaluated using X-ray diffraction (XRD) and Raman spectroscopy, respectively. First, XRD analysis (Fig. 1(d)) showed that both ZFO and F-ZFO exhibited peaks centered at 29.92°, 35.26°, 36.86°, 42.84°, 53.11°, and 56.63°, which corresponded to the (220), (311), (222), (400), (422), and (511) crystal planes of spinel zinc ferrite (JCPDS Card No. 022-1012). In addition, the calculated crystallite size (via the Scherrer equation [47]) of F-ZFO (17 nm) was larger than that of ZFO (12 nm), which is consistent with the SEM observations. Notably, F-ZFO retained a single phase of spinel zinc ferrite even after high-temperature flame treatment (reducing atmosphere). In contrast, the flame treatment in an oxidizing atmosphere resulted in phase separation into α -Fe₂O₃ and ZnO (Fig. S7 in the ESM). This result indicates that a reducing atmosphere is preferable for flame activation because the oxidizing atmosphere decomposes ZFO.

Raman spectra (Fig. 1(e)) showed that the typical E_g , F_{2g} , and A_{1g} modes were observed in ZFO and F-ZFO. Additionally, no characteristic peaks of hematite (α -Fe₂O₃, 1320 cm⁻¹) or maghemite (γ -Fe₂O₃, 1400 cm⁻¹) were observed, confirming a single phase of ZFO [31]. Notably, the absence of carbon peak (D-band at 1348 cm⁻¹ and G-band at 1603 cm⁻¹) indicates no carbon

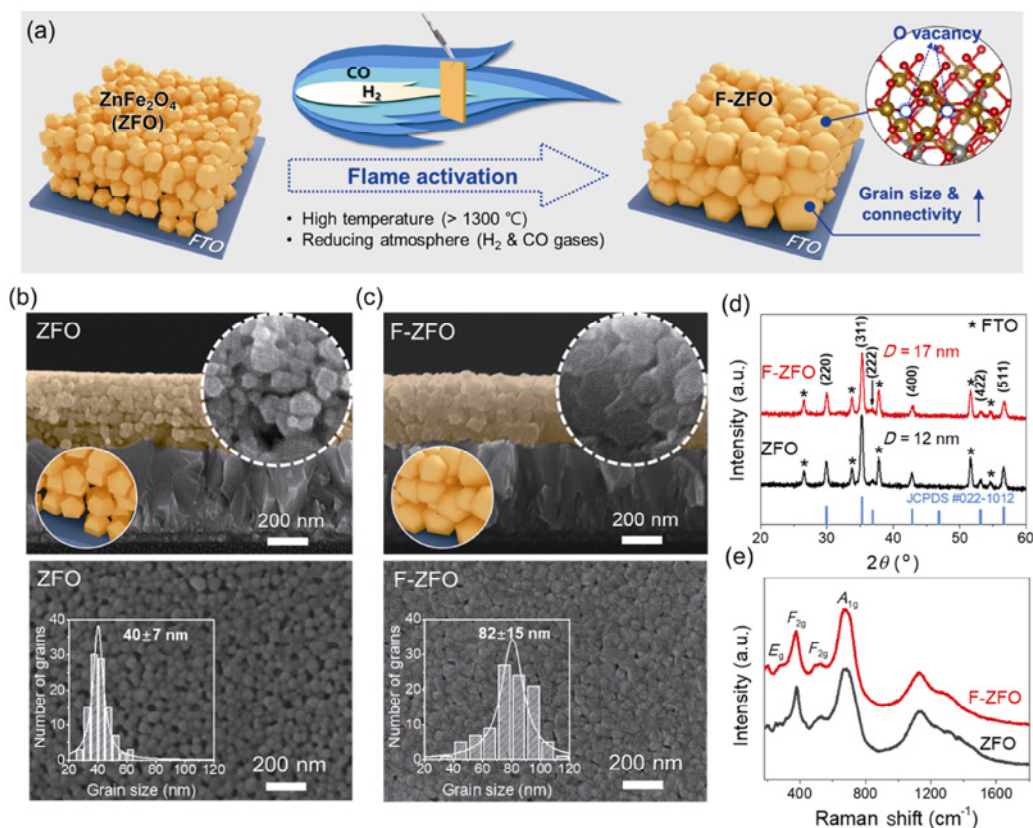


Fig. 1 Flame activation of the ZnFe_2O_4 (ZFO) photoanode. (a) Flame activation and its impacts on grain size, connectivity, and oxygen vacancy formation of ZFO. The high temperature and reducing flame promote grain fusion/growth and generate oxygen vacancy. SEM images of (b) ZFO and (c) flame-activated ZFO (F-ZFO). (d) XRD pattern and (e) Raman spectra of ZFO and F-ZFO.

species formation after flame activation (Fig. S8 in the ESM). Interestingly, all peaks in F-ZFO exhibited a slight negative shift (up to 5 cm^{-1}) compared to that of ZFO, indicating a chemical structure change or defect formation [39,42,48] due to flame activation.

3.2 Surface defects, electrochemical active surface area, and carrier concentration analyses

Surface defects, electrochemical active surface area (EASA), and carrier concentration, which are decisive factors for PEC water splitting activity, are investigated. First, X-ray photoelectron spectroscopy (XPS) analysis was performed to investigate the effect of flame activation on the formation of surface defects. The XPS O 1s spectra (Fig. 2(a)) were deconvoluted into three peaks centered at 529.5, 530.8, and 532.6 eV, which represented lattice oxygen (O_L), oxygen vacancy (O_V), and surface hydroxyl species (O_{OH}), respectively [49]. Additionally, the Fe 2p spectra (Fig. 2(b)) were deconvoluted into Fe^{2+} and Fe^{3+} peaks at 710.4 and 712.9 eV, respectively. As summarized in Fig. 2(c) and Table S2 in the ESM, the relative amounts of oxygen

vacancies and Fe^{2+} increased after flame activation. In a typical spinel ZFO structure, Zn^{2+} occupies tetrahedral sites and is bonded to four oxygen atoms, whereas Fe^{3+} occupies octahedral sites and is bonded to six oxygen atoms. Accordingly, the increase in Fe^{2+} indicates more inversion of Fe^{3+} into Fe^{2+} , that is, an increase in Fe^{2+} at the tetrahedral sites. In this case, oxygen can easily escape from the lattice structure owing to the charge compensation effect [50], thus clarifying the increase in oxygen vacancies. Moreover, the Zn 2p spectra (Fig. S9 in the ESM) show a similar peak shift after flame activation, which is also attributed to the inversion of Fe^{3+} and oxygen vacancy formation. Furthermore, The EPR signal illustrates an isotropic resonance band with $g = 2.02$ (Fig. S10 in the ESM). A stronger paramagnetic signal of F-ZFO is observed than that of ZFO, indicating increased oxygen vacancy concentration after flame activation, which agrees with the XPS results. The oxygen vacancy in metal oxide photoanode is demonstrated to affect charge carrier concentration and surface reactivity, thus improving the PEC activity [42,44,51].

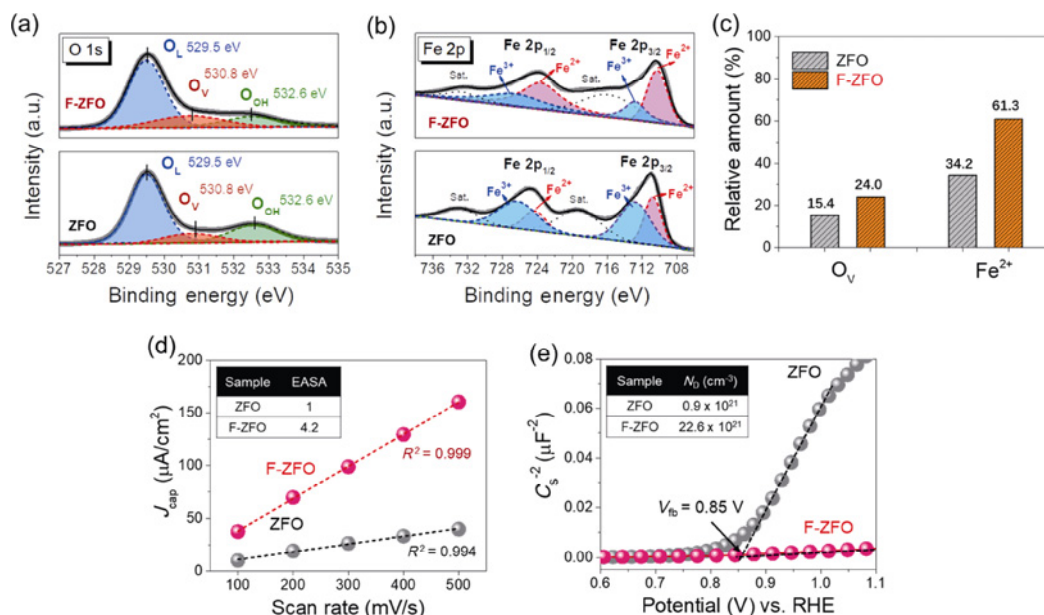


Fig. 2 Surface defects, relative surface area, and carrier concentration analyses. XPS spectra of (a) O 1s and (b) Fe 2p. (c) Relative amounts of oxygen vacancy and Fe²⁺. O_L: lattice oxygen. O_V: oxygen vacancy. Relative amount of [O_V] = [O_V]/[O_L + O_V] and [Fe²⁺] = [Fe²⁺]/[Fe³⁺ + Fe²⁺]. (d) Relative electrochemical active surface area (EASA) and (e) Mott–Schottky (MS) analysis of ZFO and F-ZFO.

The relative electrochemical active surface area (EASA) of ZFO and F-ZFO were examined by measuring the cyclic voltammetry curves at various scan rates (Fig. 2(d) and Fig. S11 in the ESM). The EASA of the F-ZFO was four times larger than that of the ZFO. Therefore, the enhanced EASA of F-ZFO is attributed to the oxygen vacancy (V_o) and charged defect (Fe²⁺) formation on the surface, which induced more adsorption and active sites, thereby strongly influencing surface reactivity [52].

The charge carrier concentrations in ZFO and F-ZFO were determined using the Mott–Schottky measurement. As shown in Fig. 2(e), both ZFO and F-ZFO exhibit positive slopes, indicating typical n-type semiconducting behavior. In addition, the flat band potential (V_{fb}) was determined to be 0.85 V vs. RHE, consistent with Ref. [23]. However, the F-ZFO exhibited a considerably lower slope than ZFO, indicating a significantly higher charge carrier concentration (N_D). The N_D value of F-ZFO ($22.6 \times 10^{21} \text{ cm}^{-3}$) was 25 times higher than that of ZFO ($0.9 \times 10^{21} \text{ cm}^{-3}$), indicating an improved n-type conductivity. In addition, the F-ZFO shows a remarkably increased electrical conductivity and decreased sheet resistivity compared to ZFO (Fig. S12 in the ESM). Resultingly, flame activation effectively generated oxygen vacancies in F-ZFO, improving the active surface area and charge carrier density.

3.3 Photoelectrochemical (PEC) activity

The photocurrent–potential (J – V) curves of ZFO and F-ZFO were measured using a three-electrode system in a 1 M NaOH (pH = 13.6) electrolyte under simulated sunlight illumination (Fig. 3(a)). As shown in Fig. 3(b), ZFO (before flame activation), exhibits a weak photocurrent response (0.03 mA/cm^2). In contrast, F-ZFO exhibited a high photocurrent density (J_{ph}) of 0.3 mA/cm^2 at 1.23 V_{RHE} , ten times higher than ZFO (Table S4 in the ESM). In particular, an impressive photocurrent density of $\sim 0.93 \text{ mA/cm}^2$ was obtained at 1.60 V vs. RHE, demonstrating that the flame activation effectively improves the photocurrent density of ZFO. However, the F-ZFO exhibits a higher onset potential than ZFO. First, the high defect concentration at the surface causes Fermi-level pinning, which leads to the delay of onset potential [37]. Second, the increased charge carrier concentration induced by oxygen vacancy decreases depletion layer width, leading to a deterioration of charge transport at the low bias potential [53].

Next, the effect of the flame atmosphere on the PEC activity was investigated (Fig. 3(c) and Fig. S13 in the ESM). The results show that the reducing flame (fuel-rich, $\phi > 1$) yields a substantially higher J_{ph} value than those of the neutral and oxidizing flames. Notably, the reducing flame is more effective than the oxidizing and neutral flame conditions in forming oxygen vacancies in ZFO, which results from the generation of reducing

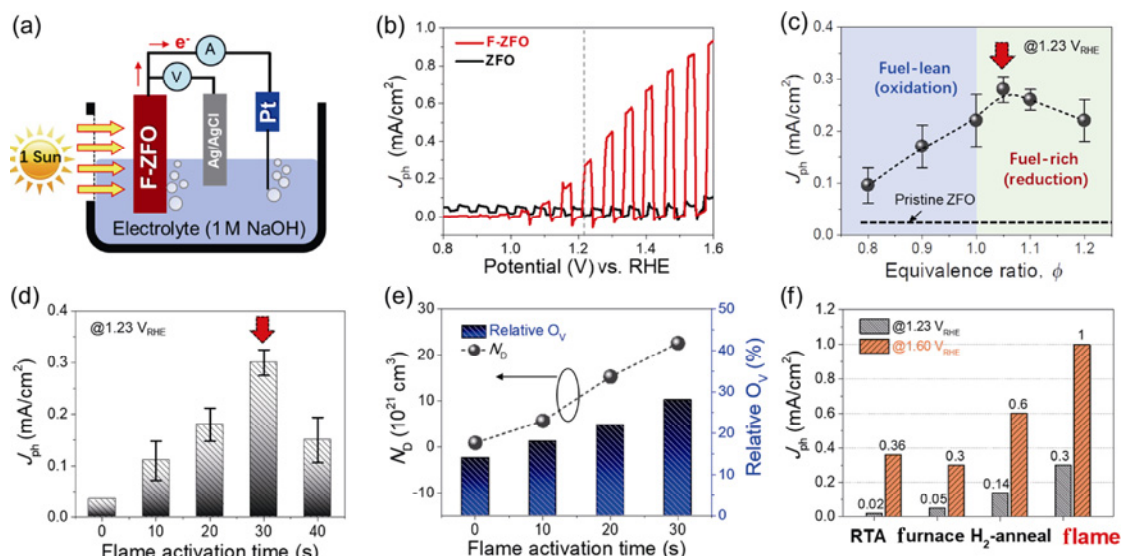


Fig. 3 Photoelectrochemical (PEC) activity. (a) Schematic of PEC cell. (b) Representative photocurrent density–potential (J – V) curves of ZFO and F-ZFO measured under simulated sunlight illumination (100 mW/cm^2). (c) Effects of the flame equivalence ratio on the photocurrent density (J_{ph} values are extracted at $1.23 V_{\text{RHE}}$ from corresponding J – V curves). (d) Effects of the flame activation time on the J_{ph} . (e) Variations of donor concentration (N_{D}) and oxygen vacancy amount (O_{V}) as a function of the flame activation time. (f) Comparison of various activation methods. Flame-activated ZFO shows the highest J_{ph} , indicating the effectiveness of flame activation in improving the PEC activity of ZFO.

gases of CO and H₂ in the reducing flame. Notably, the reducing flame at $\Phi = 1.05$ generates the highest photocurrent density and enables good repeatability (Fig. S14 in the ESM). Interestingly, the oxidizing and neutral flame activations also improved the J_{ph} values of pristine ZFO. This result indicates that increased grain size and enhanced connectivity are crucial in improving the PEC activity of ZFO (Fig. S15 in the ESM). Once oxygen vacancies are introduced in these large-grained and inter-connected ZFO, the PEC activity will be improved further due to the synergistic effect of the increase of active surface sites.

Figure 3(d) shows the J_{ph} variation as a function of flame activation time. The J_{ph} of F-ZFO increased until 30 s and then decreased at 40 s (Fig. S16 in the ESM). To elucidate this behavior, the oxygen vacancy concentration (O_{V}) and donor concentration (N_{D}) were investigated as a function of flame activation time (Fig. 3(e) and Figs. S17 and S18 in the ESM). Both N_{D} and O_{V} are increased monotonically with the increase of the flame activation time. Therefore, the increase in J_{ph} until 30 s is well correlated to the increase of N_{D} and O_{V} , suggesting that the conductivity increase resulting from the oxygen vacancy formation is responsible for the J_{ph} improvement. However, the excess amount of oxygen vacancies due to prolonged flame activation (> 30 s) leads to the formation of surface trap sites, resulting in severe charge recombination, thereby

deteriorating the J_{ph} increase [54]. The optimal thickness of F-ZFO was determined to be $\sim 600 \text{ nm}$ (Figs. S19 and S20 in the ESM). Because ZFO has a low light absorption coefficient [29], the thicker film is required to absorb sunlight effectively. Notably, further thickening of ZFO above 600 nm diminishes J_{ph} , caused by the short hole diffusion length [30] and increased bulk recombination at thicker ZFO.

To prove the effectiveness of our flame activation, other frequently employed methods, such as RTA (rapid thermal annealing), high-temperature furnace annealing, and H₂ annealing, were tested using ZFO nanoparticle films. The other methods' optimal treatment conditions were referred to in Refs. [37,42,51]. However, the thickness of the ZFO is fixed at 600 nm for all cases. As shown in Fig. 3(f) and Fig. S21 in the ESM, the methods also improve J_{ph} ; however, our flame activation produces the highest value. The RTA (heating rate: $100 \text{ }^\circ\text{C/s}$)-treated ZFO exhibited the lowest improvement in J_{ph} , which is ascribed to the low heat flux owing to the heat transport mechanism (conduction through silicon–glass–FTO–ZFO layers) [42]. Similarly, furnace activation at $800 \text{ }^\circ\text{C}$ also moderately improved J_{ph} . As shown in Fig. S22 in the ESM, J_{ph} increases with the furnace annealing temperature. However, high-temperature annealing of FTO substrates > $800 \text{ }^\circ\text{C}$ is limited because of damage to the glass and FTO layers [55].

The most popular method, H₂ annealing, achieved an enhanced J_{ph} of 0.14 and 0.6 mA/cm² at 1.23 and 1.6 V_{RHE}, respectively. According to Kim *et al.* [51] and Polo *et al.* [31,37], H₂ annealing efficiently generates oxygen vacancies via hydrogenation. Nevertheless, the flame-activated ZFO exhibited the highest J_{ph} of 0.3 and 0.93 mA/cm² at 1.23 and 1.6 V vs. RHE, respectively, demonstrating the effectiveness of our flame activation method in improving the PEC activity of ZFO.

Additionally, we tested the direct flame annealing (i.e., flame treatment at 1300 °C for 30 s without the annealing at 550 °C) of ZFO (Fig. S23 in the ESM). Interestingly, the direct flame-annealed ZFO exhibited $J-V$ curves similar to those of F-ZFO. Therefore, the flame also can be utilized as an annealing tool instead of conventional furnace annealing.

Consequently, the flame exerts two critical functions to enhance the PEC activity of the ZFO. First, the ultra-high temperature and rapid activation time (< 1 min) increase the grain size and improve grain connectivity while preserving the delicate FTO substrate from thermal damage. These characteristics are unattainable by other methods such as furnaces and RTA. Second, the reducing flame generates oxygen vacancies, which are more effective than the H₂ annealing method in terms of treatment time and controllability. Moreover, our flame was facile, ultrafast, and scalable (Fig. S24 in the ESM).

3.4 Light absorption, charge transport, and transfer kinetics studies

A series of characterizations and measurements were performed to elucidate the impacts of the increased grain size and oxygen vacancy formation in F-ZFO on the charge collection (transport and transfer) properties. The optical properties of ZFO and F-ZFO were investigated (Fig. 4(a) and Fig. S25 in the ESM). Interestingly, F-ZFO exhibited a slightly higher light absorption (77%) than that of ZFO (73%). In particular, light absorption in the longer wavelength region (500–700 nm) was enhanced. This enhanced light absorption of F-ZFO is partly attributed to the increased optical density resulting from the larger grain size and connectivity. The oxygen vacancy increase also contributed to the enhanced light absorption of F-ZFO [56]. According to Granone *et al.* [57], an increase in the inversion degree (i.e., an increase in tetrahedrally coordinated Fe²⁺) improves visible light absorption,

producing a characteristic darkening of the sample. Similarly, we observed a darker reddish-brown color of F-ZFO compared to that of ZFO (Fig. 4(a)), suggesting enhanced optical density.

For the IPCE spectra, F-ZFO exhibited substantially higher values at the wavelength region of 350–550 nm (Fig. 4(b)): the maximum IPCE values of F-ZFO and ZFO were 17.2% and 2.7%, respectively. In addition, the integrated photocurrent density matched the J_{ph} value obtained from the $J-V$ curves (Fig. 3(b)). However, no IPCE improvement was observed in the 500–600 nm wavelength region, where the light absorption was enhanced. This result indicates that light absorption has minimal impact on the improved photocurrent density of F-ZFO.

Next, EIS analysis was conducted to identify the charge transport and transfer characteristics of F-ZFO and ZFO (Fig. 4(c)). Nyquist plots were fitted using an equivalent circuit model (the inset in Fig. 4(c)). The results are summarized in Table S5 in the ESM, where R_1 , R_2 , and R_3 are the series, charge transport (in bulk ZFO), and charge transfer (at the interface between ZFO and the electrolyte) resistances, respectively; and C_1 and C_2 are the capacitances of the space charge region and Helmholtz layer, respectively. Notably, F-ZFO exhibited considerably smaller R_2 and R_3 values than those of ZFO, indicating its significantly enhanced charge transport and transfer properties. To confirm this, the charge transport ($\eta_{transport}$) and transfer ($\eta_{transfer}$) efficiencies were quantified using the hole scavenger method (Figs. 4(d), 4(e), and Fig. S26 in the ESM). First, the F-ZFO exhibited a $\eta_{transfer}$ of 20.8%, which was approximately two times higher than that of ZFO (12.4%). This enhanced $\eta_{transfer}$ is attributed to the suitable number of oxygen vacancies on the F-ZFO surface, which increased the surface area and active sites [58,59]. In addition to the $\eta_{transfer}$, F-ZFO exhibited two times higher $\eta_{transport}$ (9.3%) than that of ZFO (4.5%). As shown in the SEM, XPS, and Mott–Schottky analyses (Figs. 1 and 2), this enhancement in $\eta_{transport}$ is ascribed to the reduced grain boundary (increased grain size) and vastly increased charge carrier concentration (via the formation of oxygen vacancies), which suppress the surface and bulk recombination of charge carriers.

The charge transport time constant (τ) is a valuable factor for evaluating charge transport kinetics because it represents the speed at which the photogenerated electrons reach the FTO substrate [60]. To confirm the

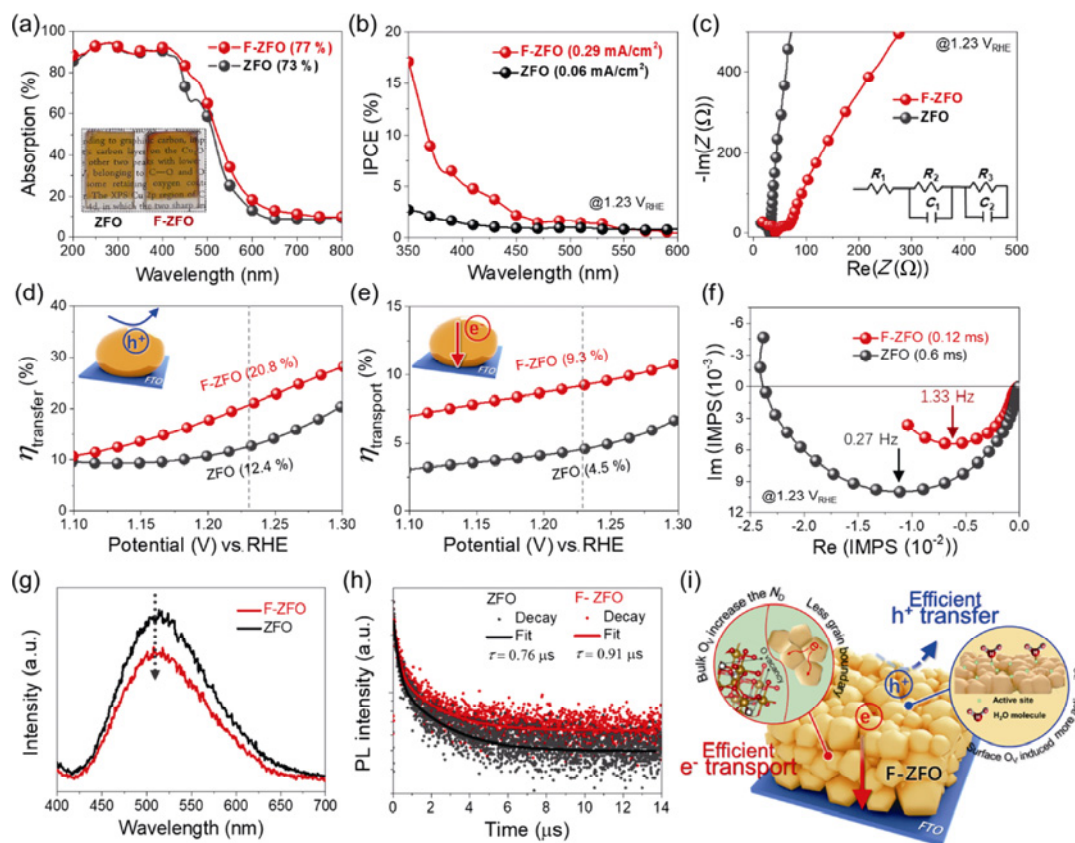


Fig. 4 Optical property, spectral response, charge transport, and transfer kinetics analyses. (a) Light absorption spectra. The inset image shows a photograph of ZFO and F-ZFO samples. (b) Incident photon to current conversion efficiency (IPEC) spectra. (c) Nyquist plot. (d) Charge transfer efficiency (η_{transfer}) and (e) charge transport efficiency ($\eta_{\text{transport}}$). (f) Intensity-modulated photocurrent spectroscopy (IMPS) spectra. (g) Photoluminescence (PL) spectra and (h) time-resolved photoluminescence (TRPL) spectra of ZFO and F-ZFO under an excitation of 374 nm. (i) Impacts of flame activation on the improvement of the charge carrier dynamics.

correlation between τ and the improved J_{ph} on F-ZFO, IMPS analysis (Fig. 4(f)) was performed at an applied potential of 1.23 V_{RHE}. The τ values of ZFO and F-ZFO were 0.6 and 0.12 ms, respectively. The five times smaller τ value of F-ZFO indicates that the photogenerated charges in F-ZFO were more efficiently collected on the FTO substrate. Consequently, F-ZFO exhibited diminished charge recombination in bulk, which improves the charge transport and J_{ph} for PEC water splitting.

Photoluminescence (PL) and time-resolved PL (TRPL) spectroscopy analyses were performed to investigate the carrier dynamics. First, the PL intensity of F-ZFO (Fig. 4(g)) was lower than that of ZFO, indicating diminished charge recombination (enhanced charge-separation properties) [61]. Furthermore, the TRPL results (Fig. 4(h) and Table S6 in the ESM) show an increased carrier lifetime (0.91 μs) in F-ZFO compared to that of ZFO (0.76 μs), suggesting the fewer defects (high crystal quality) in F-ZFO. Resultingly, as

summarized in Fig. 4(i), the reduced grain boundaries, improved connectivity, and oxygen vacancies played crucial roles in the enhanced charge transport and transfer kinetics of F-ZFO.

3.5 Further improvement of PEC activity

The PEC activity of F-ZFO was further improved by deposition of the Al₂O₃ passivation layer and NiFeO_x OEC. SEM-EDS and XPS analyses confirmed the conformal and uniform coatings of NiFeO_x and Al₂O₃ layers (Figs. S27 and S28 in the ESM). The Al₂O₃ layer was deposited between the F-ZFO and OEC by dip-coating to passivate surface defects that act as charge recombination sites. This Al₂O₃ layer promotes holes to escape from the bulk region of F-ZFO and then transfers them to the OEC layer without significant loss [36]. As shown in Fig. 5(a), the Al₂O₃/F-ZFO exhibits a higher photocurrent density than that of F-ZFO, and the optimized photocurrent density (0.52 mA/cm²) was obtained at three-cycle dip-coating (Fig. S29 in the ESM).

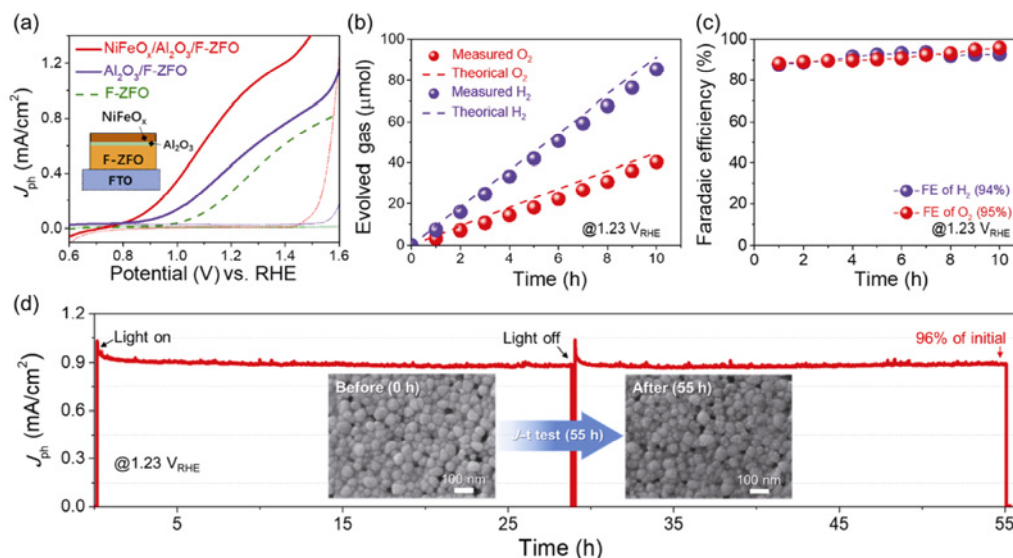


Fig. 5 Further improvement of PEC performance via depositing Al₂O₃ and NiFeO_x layers. (a) J - V curves of F-ZFO, Al₂O₃/F-ZFO, and NiFeO_x/Al₂O₃/F-ZFO photoanodes. (b) Gas production measurements. A stoichiometric mole ratio of H₂ and O₂ (H₂/O₂ = 2) was observed. (c) Faradaic efficiency (FE) measurement. (d) Long-term photocurrent stability test of the NiFeO_x/Al₂O₃/F-ZFO photoanodes. The inset images show SEM images before and after the 55 h stability test.

After deposition of NiFeO_x OEC, the fully modified NiFeO_x/Al₂O₃/F-ZFO exhibited an impressive J_{ph} of 0.95 mA/cm², which is over three times higher than F-ZFO. Moreover, it exhibited a large onset potential shift (−250 mV) from 1.0 to 0.75 V. These results clearly show that the Al₂O₃ layer and NiFeO_x OEC effectively improve the charge transfer efficiency and thus PEC activity (Fig. S30 in the ESM). Notably, the demonstrated J_{ph} value of NiFeO_x/Al₂O₃/F-ZFO was the highest among all nanoparticle-based planar ZFO photoanodes, even comparable with the state-of-art performance of previously reported ZFO (Tables S7, S8, and Fig. S31 in the ESM).

The water-splitting reaction was confirmed by measuring the amount of gas produced (Fig. 5(b) and Fig. S32 in the ESM). Both F-ZFO and NiFeO_x/Al₂O₃/F-ZFO exhibited a mole ratio of 1:2 for O₂ and H₂ gas, indicating the water-splitting reaction without any side reactions. Notably, the faradaic efficiencies of F-ZFO and NiFeO_x/Al₂O₃/F-ZFO were 82% and 95%, respectively. Remarkably, the NiFeO_x/Al₂O₃/F-ZFO exhibited excellent photocurrent stability (4% decrease) after the 55 h stability test (Fig. 5(d)). The SEM images before and after the stability test shows no changes in grain size or morphology, indicating the excellent durability of NiFeO_x/Al₂O₃/F-ZFO.

3.6 Flame activation of other spinel ferrites

Finally, the flame activation was applied to other spinel

ferrites (MgFe₂O₄, NiFe₂O₄, and CuFe₂O₄), which have rarely been studied as photoelectrodes, and the demonstrated photocurrent densities were very low [24,62]. As demonstrated in Fig. S33 in the ESM, the J_{ph} values of these spinel ferrites are significantly improved after flame activation: CuFe₂O₄ (93 times), MgFe₂O₄ (16 times), and NiFe₂O₄ (12 times). This result shows that flame activation can effectively improve the photocurrent densities of other spinel ferrites. Furthermore, similar to F-ZFO, grain size and connectivity improvements were observed in these spinel ferrites after flame activation (Fig. S34 in the ESM). In addition, no secondary phases were formed after flame activation (Fig. S35 in the ESM). Moreover, EASA analyses of the three spinel ferrites confirmed that flame activation increased the electrochemically active surface area (Fig. S36 in the ESM). As a result, a flame activation method is a versatile tool for enhancing the PEC performance of various spinel ferrites.

4 Conclusions

We developed a flame activation method for spinel ZFO to improve its PEC performance. The treatment of high-temperature flame (> 1300 °C) facilitated ZFO grain growth and fusion, reducing grain boundaries and improving grain connection without FTO damage. Furthermore, reducing gases, such as CO and H₂, in

the flame generated a controllable number of oxygen vacancies. These factors effectively increased the charge carrier concentration and active surface sites, promoting charge transport and transfer kinetics. Significantly, the flame-activated ZFO photoanode exhibited a photocurrent density that was 10-fold higher than that of the pristine ZFO photoanode. Furthermore, we demonstrated the highest photocurrent density of 0.95 mA/cm² by depositing Al₂O₃ passivation and NiFeO_x oxygen evolution catalyst layers, which is one of the highest values among all reported ZFO photoanodes. We also demonstrated that our flame activation method could be applied to other spinel ferrites (MgFe₂O₄, NiFe₂O₄, and CuFe₂O₄) to improve their PEC activities.

Acknowledgements

This research was supported by the Basic Science Research Program of the National Research Foundation of Korea, funded by the Ministry of Science, ICT, and Future Planning (Grant Nos. NRF-2019R1A2C2002024 and 2021R1A4A1031357).

Electronic Supplementary Material

Supplementary material is available in the online version of this article at <https://doi.org/10.26599/JAC.2023.9220709>.

References

- [1] Chen ZB, Dinh HN, Miller E. *Photoelectrochemical Water Splitting*. New York: Springer New York, 2013.
- [2] Yang Y, Niu SW, Han DD, *et al.* Progress in developing metal oxide nanomaterials for photoelectrochemical water splitting. *Adv Energy Mater* 2017, **7**: 1700555.
- [3] Jiang CR, Moniz SJA, Wang AQ, *et al.* Photoelectrochemical devices for solar water splitting-materials and challenges. *Chem Soc Rev* 2017, **46**: 4645–4660.
- [4] Alfaifi BY, Ullah H, Alfaifi S, *et al.* Photoelectrochemical solar water splitting: From basic principles to advanced devices. *Veruscript Funct Nanomater* 2018, **2**: BDJOC3.
- [5] He YM, Hamann T, Wang DW. Thin film photoelectrodes for solar water splitting. *Chem Soc Rev* 2019, **48**: 2182–2215.
- [6] Fountaine KT, Lewerenz HJ, Atwater HA. Efficiency limits for photoelectrochemical water-splitting. *Nat Commun* 2016, **7**: 13706.
- [7] Ge M, Li Q, Cao C, *et al.* One-dimensional TiO₂ nanotube photocatalysts for solar water splitting. *Adv Sci: Weinh* 2017, **4**: 1600152.
- [8] Cho IS, Chen ZB, Forman AJ, *et al.* Branched TiO₂ nanorods for photoelectrochemical hydrogen production. *Nano Lett* 2011, **11**: 4978–4984.
- [9] Ma M, Zhang K, Li P, *et al.* Dual oxygen and tungsten vacancies on a WO₃ photoanode for enhanced water oxidation. *Angew Chem Int Ed Engl* 2016, **55**: 11819–11823.
- [10] Wang YD, Tian W, Chen C, *et al.* Tungsten trioxide nanostructures for photoelectrochemical water splitting: Material engineering and charge carrier dynamic manipulation. *Adv Funct Mater* 2019, **29**: 1809036.
- [11] McDonald KJ, Choi KS. A new electrochemical synthesis route for a BiOI electrode and its conversion to a highly efficient porous BiVO₄ photoanode for solar water oxidation. *Energy Environ Sci* 2012, **5**: 8553–8557.
- [12] Kim TW, Choi KS. Nanoporous BiVO₄ photoanodes with dual-layer oxygen evolution catalysts for solar water splitting. *Science* 2014, **343**: 990–994.
- [13] Han HS, Shin S, Kim DH, *et al.* Boosting the solar water oxidation performance of a BiVO₄ photoanode by crystallographic orientation control. *Energy Environ Sci* 2018, **11**: 1299–1306.
- [14] Lin YJ, Yuan GB, Sheehan S, *et al.* Hematite-based solar water splitting: Challenges and opportunities. *Energy Environ Sci* 2011, **4**: 4862–4869.
- [15] Cho IS, Han HS, Logar M, *et al.* Solar water splitting: Enhancing low-bias performance of hematite photoanodes for solar water splitting by simultaneous reduction of bulk, interface, and surface recombination pathways. *Adv Energy Mater* 2016, **6**: 1501840.
- [16] Zhang HM, Li DF, Byun WJ, *et al.* Gradient tantalum-doped hematite homojunction photoanode improves both photocurrents and turn-on voltage for solar water splitting. *Nat Commun* 2020, **11**: 4622.
- [17] Liu J, Zeng M, Yu RH. Surfactant-free synthesis of octahedral ZnO/ZnFe₂O₄ heterostructure with ultrahigh and selective adsorption capacity of malachite green. *Sci Rep* 2016, **6**: 25074.
- [18] Taffa DH, Dillert R, Ulpe AC, *et al.* Photoelectrochemical and theoretical investigations of spinel type ferrites (M_xFe_{3-x}O₄) for water splitting: A mini-review. *J Photon Energy* 2017, **7**: 012009.
- [19] Chandrasekaran S, Bowen C, Zhang PX, *et al.* Spinel photocatalysts for environmental remediation, hydrogen generation, CO₂ reduction and photoelectrochemical water splitting. *J Mater Chem A* 2018, **6**: 11078–11104.
- [20] Zhu XD, Guijarro N, Liu YP, *et al.* Spinel structural disorder influences solar-water-splitting performance of ZnFe₂O₄ nanorod photoanodes. *Adv Mater* 2018, **30**: 1801612.
- [21] Kim ES, Nishimura N, Magesh G, *et al.* Fabrication of CaFe₂O₄/TaON heterojunction photoanode for photoelectrochemical water oxidation. *J Am Chem Soc* 2013, **135**: 5375–5383.
- [22] Ida S, Yamada K, Matsunaga T, *et al.* Preparation of p-type CaFe₂O₄ photocathodes for producing hydrogen from water. *J Am Chem Soc* 2010, **132**: 17343–17345.

- [23] Henning RA, Uredat P, Simon C, *et al.* Characterization of MFe_2O_4 ($M = Mg, Zn$) thin films prepared by pulsed laser deposition for photoelectrochemical applications. *J Phys Chem C* 2019, **123**: 18240–18247.
- [24] Guijarro N, Borno P, Prévot M, *et al.* Evaluating spinel ferrites MFe_2O_4 ($M = Cu, Mg, Zn$) as photoanodes for solar water oxidation: Prospects and limitations. *Sustainable Energy Fuels* 2018, **2**: 103–117.
- [25] Park S, Baek JH, Zhang L, *et al.* Rapid flame-annealed $CuFe_2O_4$ as efficient photocathode for photoelectrochemical hydrogen production. *ACS Sustainable Chem Eng* 2019, **7**: 5867–5874.
- [26] Maitra S, Pal S, Maitra T, *et al.* Solvothermal etching-assisted phase and morphology tailoring in highly porous $CuFe_2O_4$ nanoflake photocathodes for solar water splitting. *Energy Fuels* 2021, **35**: 14087–14100.
- [27] Doiphode V, Vairale P, Sharma V, *et al.* Solution-processed electrochemical synthesis of $ZnFe_2O_4$ photoanode for photoelectrochemical water splitting. *J Solid State Electrochem* 2021, **25**: 1835–1846.
- [28] Park JW, Mahadik MA, An GW, *et al.* Activation of a highly oriented columnar structure of $ZnFe_2O_4$ for photoelectrochemical water splitting: Orchestrated effects of two-step quenching and Sn^{4+} diffusion. *Sol Energy Mater Sol Cells* 2018, **187**: 207–218.
- [29] Hufnagel AG, Peters K, Müller A, *et al.* Zinc ferrite photoanode nanomorphologies with favorable kinetics for water-splitting. *Adv Funct Mater* 2016, **26**: 4435–4443.
- [30] Liu YP, Xia M, Yao L, *et al.* Spectroelectrochemical and chemical evidence of surface passivation at zinc ferrite ($ZnFe_2O_4$) photoanodes for solar water oxidation. *Adv Funct Mater* 2021, **31**: 2010081.
- [31] Polo A, Lhermitte CR, Dozzi MV, *et al.* Hydrogenation of $ZnFe_2O_4$ flat films: Effects of the pre-annealing temperature on the photoanodes efficiency for water oxidation. *Surfaces* 2020, **3**: 93–104.
- [32] Kim JH, Kim JH, Jang JW, *et al.* Awakening solar water-splitting activity of $ZnFe_2O_4$ nanorods by hybrid microwave annealing. *Adv Energy Mater* 2015, **5**: 1401933.
- [33] Anushkaran P, Mahadik MA, Hwang JB, *et al.* Synchronized effect of *in-situ* Ti doping and microwave-assisted SiO_x hole transport channel on $ZnFe_2O_4$ nanocoral arrays for efficient photoelectrochemical water splitting. *Appl Surf Sci* 2022, **592**: 153212.
- [34] Guo YS, Zhang NS, Wang X, *et al.* A facile spray pyrolysis method to prepare Ti-doped $ZnFe_2O_4$ for boosting photoelectrochemical water splitting. *J Mater Chem A* 2017, **5**: 7571–7577.
- [35] Kim JH, Jang YJ, Choi SH, *et al.* A multitude of modifications strategy of $ZnFe_2O_4$ nanorod photoanodes for enhanced photoelectrochemical water splitting activity. *J Mater Chem A* 2018, **6**: 12693–12700.
- [36] Kim JH, Choi IY, Kim JH, *et al.* $ZnFe_2O_4$ dendrite/ SnO_2 helix 3D hetero-structure photoanodes for enhanced photoelectrochemical water splitting: Triple functions of SnO_2 nanohelix. *Small* 2021, **17**: 2103861.
- [37] Polo A, Boudoire F, Lhermitte CR, *et al.* Key factors boosting the performance of planar $ZnFe_2O_4$ photoanodes for solar water oxidation. *J Mater Chem A* 2021, **9**: 27736–27747.
- [38] Chen BY, Li D, Chen X, *et al.* Efficient and controllable flame method to generate rich oxygen vacancies in WO_3 nanosheet arrays to enhance solar water oxidation. *Appl Phys Lett* 2022, **120**: 253901.
- [39] Shao CY, Malik AS, Han JF, *et al.* Oxygen vacancy engineering with flame heating approach towards enhanced photoelectrochemical water oxidation on WO_3 photoanode. *Nano Energy* 2020, **77**: 105190.
- [40] Chen BY, Li D, Yang ZD, *et al.* Ultra-efficient post-treatment flame method to introduce abundant oxygen vacancies in $BiVO_4$ photoanode toward solar water splitting. *Chem Eng Sci* 2022, **251**: 117433.
- [41] Cho IS, Lee CH, Feng YZ, *et al.* Codoping titanium dioxide nanowires with tungsten and carbon for enhanced photoelectrochemical performance. *Nat Commun* 2013, **4**: 1723.
- [42] Cho IS, Logar M, Lee CH, *et al.* Rapid and controllable flame reduction of TiO_2 nanowires for enhanced solar water-splitting. *Nano Lett* 2014, **14**: 24–31.
- [43] Kuang YB, Jia QX, Ma GJ, *et al.* Ultraprecise low-bias water splitting photoanodes via photocorrosion inhibition and *in situ* catalyst regeneration. *Nat Energy* 2017, **2**: 16191.
- [44] Kim S, Mahadik MA, Chae WS, *et al.* Synthesis of transparent Zr-doped $ZnFe_2O_4$ nanocorals photoanode and its surface modification via $Al_2O_3/Co-Pi$ for efficient solar water splitting. *Appl Surf Sci* 2020, **513**: 145528.
- [45] Hu JF, Wang XH, Zhang JZ, *et al.* A general mechanism of grain growth - I. Theory. *J Materiomics* 2021, **7**: 1007–1013.
- [46] Hu JF, Zhang JZ, Wang XH, *et al.* A general mechanism of grain growth-II: Experimental. *J Materiomics* 2021, **7**: 1014–1021.
- [47] Lemine OM, Bououdina M, Sajieddine M, *et al.* Synthesis, structural, magnetic and optical properties of nanocrystalline $ZnFe_2O_4$. *Phys B Condens Matter* 2011, **406**: 1989–1994.
- [48] Badreldin A, Abusrafa AE, Abdel-Wahab A. Oxygen-deficient cobalt-based oxides for electrocatalytic water splitting. *ChemSusChem* 2021, **14**: 10–32.
- [49] Jain S, Shah J, Negi NS, *et al.* Significance of interface barrier at electrode of hematite hydroelectric cell for generating ecpower by water splitting. *Int J Energy Res* 2019, **43**: 4743–4755.
- [50] Chawla A, Singh A, Babu PD, *et al.* Magnetic ion oxidation state dependent magnetoelectric coupling strength in Fe doped BCT ceramics. *RSC Adv* 2020, **10**: 21019–21027.
- [51] Kim JH, Jang YJ, Kim JH, *et al.* Defective $ZnFe_2O_4$ nanorods with oxygen vacancy for photoelectrochemical water splitting. *Nanoscale* 2015, **7**: 19144–19151.
- [52] Polarz S, Strunk J, Ischenko V, *et al.* On the role of oxygen defects in the catalytic performance of zinc oxide. *Angew Chem Int Ed Engl* 2006, **45**: 2965–2969.
- [53] Zhang ZJ, Nagashima H, Tachikawa T. Ultra-narrow

- depletion layers in a hematite mesocrystal-based photoanode for boosting multihole water oxidation. *Angew Chem Int Ed Engl* 2020, **59**: 9047–9054.
- [54] Corby S, Francàs L, Selim S, *et al.* Water oxidation and electron extraction kinetics in nanostructured tungsten trioxide photoanodes. *J Am Chem Soc* 2018, **140**: 16168–16177.
- [55] Annamalai A, Subramanian A, Kang U, *et al.* Activation of hematite photoanodes for solar water splitting: Effect of FTO deformation. *J Phys Chem C* 2015, **119**: 3810–3817.
- [56] Li YZ, Li Y, Xu XM, *et al.* Structural disorder controlled oxygen vacancy and photocatalytic activity of spinel-type minerals: A case study of ZnFe₂O₄. *Chem Geol* 2019, **504**: 276–287.
- [57] Granone LI, Ulpe AC, Robben L, *et al.* Effect of the degree of inversion on optical properties of spinel ZnFe₂O₄. *Phys Chem Chem Phys* 2018, **20**: 28267–28278.
- [58] Wang ZL, Wang LZ. Role of oxygen vacancy in metal oxide based photoelectrochemical water splitting. *EcoMat* 2021, **3**: e12075.
- [59] Hu J, Zhao X, Chen W, *et al.* Enhanced charge transport and increased active sites on α -Fe₂O₃ (110) nanorod surface containing oxygen vacancies for improved solar water oxidation performance. *ACS Omega* 2018, **3**: 14973–14980.
- [60] Kwon HC, Yang W, Lee D, *et al.* Investigating recombination and charge carrier dynamics in a one-dimensional nanopillared perovskite absorber. *ACS Nano* 2018, **12**: 4233–4245.
- [61] Jing LQ, Qu YC, Wang BQ, *et al.* Review of photoluminescence performance of nano-sized semiconductor materials and its relationships with photocatalytic activity. *Sol Energy Mater Sol Cells* 2006, **90**: 1773–1787.
- [62] Soto-Arreola A, Huerta-Flores AM, Mora-Hernández JM, *et al.* Comparative study of the photocatalytic activity for hydrogen evolution of MFe₂O₄ (M = Cu, Ni) prepared by three different methods. *J Photochem Photobiol A Chem* 2018, **357**: 20–29.

Open Access This article is licensed under a Creative Commons Attribution 4.0 International License, which permits use, sharing, adaptation, distribution and reproduction in any medium or format, as long as you give appropriate credit to the original author(s) and the source, provide a link to the Creative Commons licence, and indicate if changes were made.

The images or other third party material in this article are included in the article's Creative Commons licence, unless indicated otherwise in a credit line to the material. If material is not included in the article's Creative Commons licence and your intended use is not permitted by statutory regulation or exceeds the permitted use, you will need to obtain permission directly from the copyright holder.

To view a copy of this licence, visit <http://creativecommons.org/licenses/by/4.0/>.

